Inorganic Chemistry

Article

pubs.acs.org/IC

Soft-Chemical Exfoliation of $RbSrNb_2O_6F$ into Homogeneously Unilamellar Oxyfluoride Nanosheets

Tadashi C. Ozawa,*[,†,‡] Katsutoshi Fukuda,[†,‡] Yasuo Ebina,[†,‡] and Takayoshi Sasaki[†,‡]

[†]International Center for Materials Nanoarchitectonics (WPI-MANA), National Institute for Materials Science (NIMS), 1-1 Namiki, Tsukuba, Ibaraki 305-0044, Japan

[‡]CREST, Japan Science and Technology Agency (JST), 4-1-8 Honcho, Kawaguchi, Saitama 332-0012, Japan

Supporting Information

ABSTRACT: Interlayer Rb^+ of the perovskite-type layered oxyfluoride $RbSrNb_2O_6F$ was ion-exchanged with H^+, and the protonated phase was reacted with aqueous solution of tetrabutylammonium hydroxide to exfoliate it into nanosheets. The resulting nanosheet suspension exhibits Tyndall scattering of a laser beam, indicating its colloidal nature. Elemental composition of the nanosheet was estimated as $Sr_{0.98}Nb_2O_6F_{0.97}^{\delta-}$, which was quite close to that of the layer unit of the precursor. The homogeneously unilamellar nature of this nanosheet was confirmed by atomic force and transmission electron microscopy observations and X-ray scattering results. The optical absorption edge of the nanosheet suspension was observed around at 293 nm, and two well-defined peaks with their maxima at 229 and 278 nm were observed. Furthermore, the aqueous suspension of the nanosheet exhibits fluorescence emission in the UV-blue region. These properties of the oxyfluoride nanosheets are quite different from those of its oxide analogues without F^-, such as $LnNb_2O_7^-$ nanosheets (Ln = La^{3+}, Eu^{3+}, Sm^{3+}), suggesting that anion-site replacement of oxide nanosheets can be utilized to optimize or induce various properties.

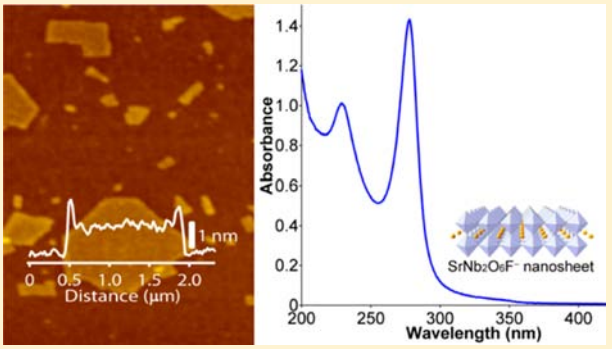

INTRODUCTION

In the past few decades, various types of oxide and nonoxide nanosheets have been reported.[1−6] Among them, soft-chemically exfoliated homogeneously unilamellar nanosheets are particularly interesting and important because of their discretely defined unique morphology consisting of μm-order lateral size and less than a few nm thickness.[5,6] The homogeneously unilamellar nature of those nanosheets is quite important when transforming nanosheets into other nanostructures, such as nanotubes, nanocones, and nanohollowed-spherical-shells, to optimize their properties and active surface area.[7−9] Furthermore, for superlattice structure fabrication via sequential deposition of various kinds of nanosheets, the unilamellar nature of the nanosheets as building blocks is a crucial aspect to realize well-defined discrete stacking.[10−12] It has been experimentally shown that soft-chemical exfoliation of bulk layered compounds is much more effective than mechanical exfoliation to obtain bona fide homogeneously unilamellar nanosheets.[2,5,13]

To date, many kinds of soft-chemically exfoliated homogeneously unilamellar nanosheets have been reported. In addition, it has been shown that chemical doping of cation sites in nanosheets with various active elements induces diverse range of functionalities in those nanosheets. Some of those functionalities are unique in the nanosheets and different from those in bulk materials. For example, Sm^{3+}-doped $LaNb_2O_7^-$ nanosheet exhibits host excitation-mediated photoluminescence that is not observed in its bulk precursor,[14] and Co^{2+}-doped titania nanosheet exhibits ferromagnetic property and high transmittance of visible light.[15] In case of bulk oxides, anion-site doping or replacement has been proved very effective and interesting, often inducing functionalities that cannot be induced via cation-site doping or replacement.[16,17] For example, anion-site doping was utilized in $(Ga_{1-x}Zn_x)(N_{1-x}O_x)$ to engineer superior performance in photocatalyst releasing hydrogen from water in sunlight.[18] Therefore, anion-site substitution must also be interesting for oxide nanosheets.

Thus far, exfoliation of a F^--incorporated layered perovskite-type oxide K_2NbO_3F has been reported.[19] However, all F^- was lost from the NbO_3F^{2-} layer unit after the exfoliation of K_2NbO_3F in water, and the resulting nanosheets were self-assembled into $KNbO_3$ particles. Thus, homogeneously unilamellar oxyfluoride nanosheets were not obtained through this approach. In addition, exfoliation of nitrogen- and/or sulfur-doped layered titania and fluorine-doped $RbLaNb_2O_7$ has been reported.[20−22] For these attempts, anion-dopants were incorporated into the bulk oxide precursors by heating them with anion-dopant sources such as NH_3, thiourea, and polytetrafluoroethylene. These approaches utilizing the post-

Received: October 11, 2012
Published: December 14, 2012

processing of nanosheet precursors limited the anion-dopant concentrations in the precursors to be very low; thus, the anion-dopant concentrations in the exfoliated nanosheets were also very low (approximately 2.8 atom % for $Ti_{0.91}O_{2-x}N_x^{\delta-}$ nanosheet) or not characterized.[20−22]

It would be interesting and important to develop new types of homogeneously unilamellar mixed-anion nanosheets, which are stoichiometrically incorporating both oxide and not a trace amount of nonoxide anions, to expand the nanosheet library for various applications and to explore the characteristics of mixed-anion nanosheets. It is expected that such nonoxide anion incorporation into a diverse family of oxide nanosheets enables tuning of physical properties via mechanisms such as modifications of crystal structures and band structures and rebalancing of charges. Particularly, nonoxide anion incorporated oxide nanosheets with perovskite-type structures are interesting for systematic characterizations of structure−property relationships.

In this study, we have attempted to prepare a homogeneously unilamellar perovskite-type oxyfluoride nanosheet by soft-chemical exfoliation of heavily F^--incorporated layered perovskite, which was directly synthesized by solid state reaction of $SrNb_2O_6$ and RbF. We have previously studied the preparation and characterizations of soft-chemically exfoliated homogeneously unilamellar $LnNb_2O_7^-$ nanosheets (Ln = La, Eu, Sm);[14,23,24] thus, we used this type of nanosheet as the fundamental unit. The first step of our approach in preparing a perovskite-type oxyfluoride nanosheet was to prepare F^--incorporated $ALaNb_2O_7$ (A = alkali-metal) as a bulk precursor. Replacement of O^{2-} with F^- requires replacement of Ln^{3+} or Nb^{5+} with a lower valent ion to maintain the charge neutrality of the compound. The previously known phase $RbSrNb_2O_6F$ satisfies such conditions;[25] thus, we prepared this compound as a precursor and attempted its soft-chemical exfoliation into homogeneously unilamellar oxyfluoride nanosheets. Detailed preparation procedures and properties of the exfoliated nanosheets are presented.

EXPERIMENTAL SECTION

Material Synthesis. The bulk layered precursor $RbSrNb_2O_6F$ was prepared by solid state reaction of $SrNb_2O_6$ and RbF similar to the previously reported method.[25] $SrNb_2O_6$ was synthesized by mixing a stoichiometric amount of $SrCO_3$ and Nb_2O_5, and heating the mixture at 1000 °C in air for 24 h. Then, 1:2 mol ratio of $SrNb_2O_6$ and RbF was mixed in an argon filled glovebox, placed in an alumina crucible, vacuum sealed in a fused-silica tube, and heated at 650 °C for 24 h. The excess RbF was used to assist the formation of the oxyfluoride product. The product was washed with water to dissolve the excess RbF component, and dried in air.

$RbSrNb_2O_6F$ was then reacted with 1 M aqueous solution of HCl at room temperature to exchange interlayer Rb^+ with H^+. This protonation process was necessary to activate the layered oxyfluoride precursor for the following exfoliation step utilizing an acid−base reaction. The ratio of $RbSrNb_2O_6F$ and the solution of HCl was fixed at 1 g/100 mL, and reaction duration was optimized between one to four days. After each day of reaction, HCl solution was decanted, and a new batch of HCl solution was added. The protonated samples were recovered by rinsing with water and drying in air.

The proton-exchanged layered oxyfluoride precursor was then reacted with an aqueous solution of tetrabutylammonium hydroxide (TBAOH). The ratio of the protonated layered oxyfluoride precursor and TBAOH solution was fixed at 0.4 g/100 mL, and the concentration of TBAOH solution was adjusted so that the mol of TBA^+ in the solution was equivalent to the mol of the interlayer H^+ in the protonated layered oxyfluoride precursor. After 17 days of vigorous shaking, a translucent white colloidal nanosheet suspension was obtained. This as-prepared nanosheet suspension was centrifuged at 2500 rpm for 5 min to separate the unexfoliated residue as sediment and the rest of the nanosheet suspension for characterizations.

Measurements and Analysis. Powder X-ray diffraction (XRD) profiles of the pristine and protonated bulk precursors and dried nanosheet suspension were obtained using Cu Kα radiation on a Rigaku RINT2200V/PC diffractometer. The diffraction peaks of the bulk layered precursors were indexed, and the lattice parameters were refined using APPLEMAN software.[26] The previously reported structural data of $RbSrNb_2O_6F$ were used as the starting parameters for the refinement.[25] The elemental compositions of the precursors and the nanosheet product were analyzed by flame atomic absorption spectrometry for Rb, inductively coupled plasma-optical emission spectrometry for Sr and Nb, and the lanthanum-alizarin complexone method for F (see the Supporting Information for details). The hydration amount of the protonated bulk layered precursor was examined by thermogravimetric (TG) analysis on a Rigaku Thermo Plus TG8120 at a heating rate of 10 °C min^{-1} in 20 mL min^{-1} flow of air. Morphology observations of the pristine and protonated bulk layered precursors were performed by scanning electron microscopy (SEM) using a Keyence VE-8800. The morphology analysis of the nanosheets was performed by atomic force microscopy (AFM) using a Seiko Instruments SPA-400 AFM system with a Si tip cantilever (20 N m^{-1}) in the dynamic force microscopy (DFM) mode. The sample for this analysis was prepared by depositing the diluted nanosheet suspension on a Si substrate coated with a polyvinylamine-polyvinylalcohol diblock copolymer as cationic electrostatic glue.[27−30] Transmission electron microscopy (TEM) observation and selected-area electron diffraction (SAED) analysis of the nanosheet were performed on a JEOL JEM-2100F transmission electron microscope at an accelerating voltage of 200 kV. The specimen for this characterization was prepared by dropping a 1000-fold diluted nanosheet suspension on a carbon microgrid and drying it. The XRD pattern of the concentrated glue-like nanosheet suspension was obtained using Cu Kα radiation on a Rigaku RINT2100 diffractometer. The aqueous suspension of the nanosheets was centrifuged at 30000 rpm for 30 min, and the supernatant was decanted. The remaining glue-like concentrated nanosheet suspension was used as the sample. The increase in the nanosheet concentration was necessary to minimize the halo pattern of the water medium in the diffraction profile. The diffraction data were acquired under a relative humidity of 95% to minimize the restacking of the nanosheets by drying. UV−vis absorption spectra of the diluted nanosheet suspensions were measured on a Hitachi U-4100 spectrophotometer. The optical absorption edge of the nanosheet was estimated by extrapolating the sharply rising portion of the spectrum to the horizontal axis, representing the wavelength. Finally, fluorescence spectra were obtained using a Hitachi F-7000 fluorescence spectrophotometer at room temperature. The emission spectra were corrected for the spectral response of the instrument using a substandard light source.

RESULTS AND DISCUSSION

The powder XRD profile of $RbSrNb_2O_6F$ is shown in Figure 1a. All of the diffraction peaks were indexed based on the previously reported tetragonal structure of $RbSrNb_2O_6F$;[25] thus, it was single phase. The refined lattice parameters (shown in Figure 1) were very close to the previously reported values, and their differences were less than 0.2%. The structure of $RbSrNb_2O_6F$ consists of perovskite-type $SrNb_2O_6F^-$-layer interspersed with Rb^+. On the basis of the powder XRD, ^{19}F MAS NMR, and calculations of lattice energy and bond valence sum, Choy et al. concluded that F^- in the $SrNb_2O_6F^-$-layer is statistically distributed with O^{2-} in O_{center} and $O_{equatorial}$ sites (Figure 2).[25]

To activate $RbSrNb_2O_6F$ for the following exfoliation reaction, the interlayer Rb^+ of $RbSrNb_2O_6F$ was ion-exchanged

dx.doi.org/10.1021/ic3022276 | Inorg. Chem. 2013, 52, 415−422

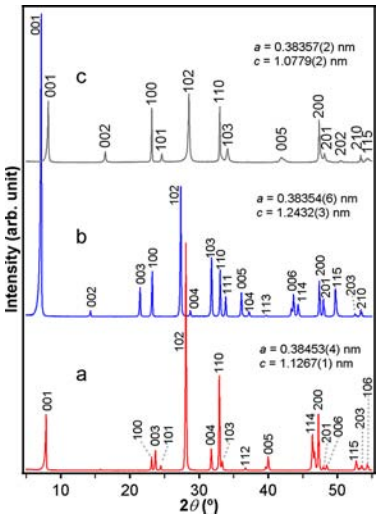

Figure 1. Powder XRD profiles of (a) as-prepared bulk layered compound precursor $RbSrNb_2O_6F$ and its protonated forms (b) dried at room temperature and (c) heated at 350 °C (after TG analysis).

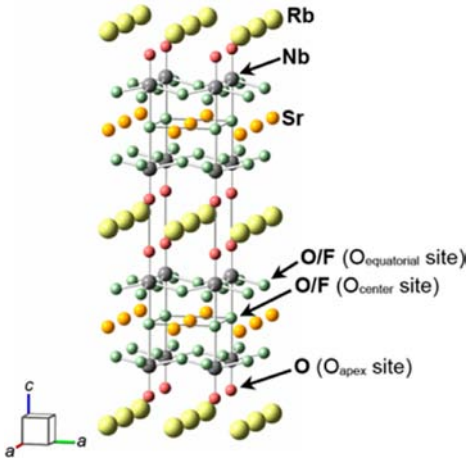

Figure 2. Crystal structure of $RbSrNb_2O_6F$.

with H^+ by reacting it with 1 M aqueous solution of HCl. The amount of Rb content remaining after each protonation reaction is shown in Table 1. While the contents of Sr and F did not decrease significantly, that of Rb decreased down to 17.4% of the pristine phase after the first protonation reaction. Further protonation reaction did cause the decrease in Rb content, but it was very gradual. The XRD profile of the bulk layered precursor after four protonation reactions is shown in Figure 1b. While the difference between the in-layer lattice parameters of the pristine and protonated precursors was less than 0.3%, the lattice parameter along the layer stacking direction of the protonated precursor was much larger than that of the pristine precursor. This is attributed to the larger interlayer spacing of the protonated phase because of the interlayer hydration; thus, a large decrease in the lattice parameter *c* was observed by dehydration upon heating (Figure 1c). This behavior was consistent with the following TG analysis results.

Table 1. Analytically Determined Molar Elemental Compositions of the Bulk Layered Precursors after Each Protonation Reaction, and Nanosheet Suspension

number of reactions	Rb	Sr	Nb	F
1	0.174	0.986	2	0.986
2	0.103	0.980	2	0.970
3	0.073	0.978	2	0.968
4	0.059	0.978	2	0.966
nanosheet suspension		0.98	2	0.94

The TG curve of the bulk layered precursor after four protonation reactions is shown in Figure 3. Sharp decrease in weight from room temperature to approximately 70 °C is attributed to the dehydration consistent with the previously mentioned results of the powder XRD. From the chemical analysis, this weight loss, and charge neutrality, the chemical formula of the bulk layered precursor after four protonation reactions was estimated as $Rb_{0.06}H_{0.94}Sr_{0.98}Nb_2O_6F_{0.97}\cdot 1.4H_2O$. For this estimation, three assumptions were made. First, there was no decrease in O content. Second, charge neutrality of the compound was maintained. Third, the oxidation state of Nb stayed as 5+. The TG trend of this protonated oxyfluoride layered precursor is different from those of other protonated layered perovskite-type oxides containing no F^-. In case of the latters, the decrease in weight was more gradual and continued to above 350 °C because of the combined contributions from the dehydration and dehydroxylation.[14,23,30,31] On the other hand, the weight decrease of the former was sharp, and no significant change in weight was observed at higher temperature up to 300 °C. This difference might be related to the effect of F^- in the structure of the former, but conclusive understanding of such aspect requires further studies. The TG curve above 300 °C was not measured to avoid the possible generation of fluorine-containing harmful gas during the experiment.

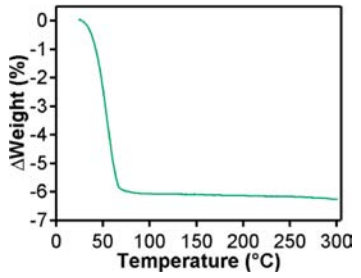

Figure 3. TG curve of the bulk layered precursor after four protonation reactions.

The SEM images of the pristine and protonated bulk layered precursors (after four protonation reactions) are shown in Figure 4. The crystallites of the pristine precursor are platelets reflecting their layered crystal structure. The majority of them are 0.5−6 μm in size. These features of the pristine precursor

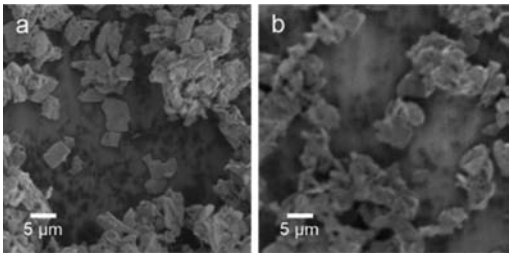

Figure 4. SEM images of (a) as-prepared bulk layered compound precursor $RbSrNb_2O_6F$ and (b) its protonated form.

dx.doi.org/10.1021/ic3022276 | *Inorg. Chem.* 2013, 52, 415−422

were retained after its protonation, indicating the topotactic nature of the protonation reaction.

The bulk layered precursor that was proton-exchanged four times was successfully exfoliated into nanosheets by reacting it with aqueous solution of TBAOH. The ratio between the protonated bulk precursor and TBAOH solution was fixed at 0.4 g/100 mL, and the concentration of TBAOH in the solution was optimized in terms of the molar ratio between the interlayer H^+ in the precursor and TBA^+ in the TBAOH solution. Among three solutions with $TBA^+/H^+ = 0.5$, 1, and 5 reacted with the precursor for 1 week, the reaction with the $TBA^+/H^+ = 1$ solution yielded the least amount of unexfoliated sediment. However, not all the nanosheets in that product were unilamellar based on the preliminary morphology observation by AFM). Thus, the reaction duration was extended to 17 days to attain complete exfoliation of the protonated precursor into homogeneously unilamellar nanosheets. Furthermore, unexfoliated residue was separated from the nanosheet suspension product by moderate-speed centrifugation for all the following characterizations. A photograph of such aqueous suspension of the nanosheet product is shown in Figure 5. It is translucent and exhibits the Tyndall effect by the scattering of a laser beam because of its colloidal nature.

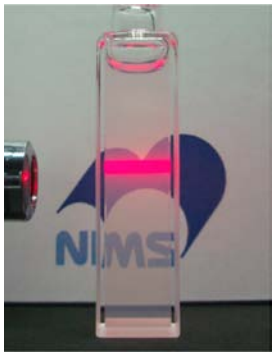

Figure 5. Photograph of a colloidal suspension of the nanosheets exfoliated from the protonated $RbSrNb_2O_6F$.

The result of the elemental composition analysis on the nanosheet suspension is shown in Table 1. For the analysis of F content, a small portion of the sample could not be removed from a sample container after the ashing preprocess required for the analysis; thus, the value in the table is likely smaller than actual one. Nevertheless, the elemental composition of the nanosheet was close to those of the pristine and protonated bulk precursors, suggesting that the $SrNb_2O_6F^-$-layer unit of the bulk layered precursors was fundamentally retained in the exfoliated nanosheet. On the other hand, small but finite amounts of Sr and F loss from the $SrNb_2O_6F^-$-layer unit were certainly observed after the protonation of the pristine bulk layered precursor $RbSrNb_2O_6F$. The amounts of Sr and F loss are roughly the same while their oxidation states are 2+ and 1−, respectively. To maintain charge neutrality of the system, additional cationic species are necessary, assuming no loss in the O^{2-} content. TBA^+, H^+, and/or H_3O^+ must be those charge compensating counterions. On the basis of these considerations, the chemical composition of the nanosheet prepared in this study was estimated to be $Sr_{0.98}Nb_2O_6F_{0.97}^{\delta-}$ where δ is approximately 1. This composition is quite close to the nominal elemental composition of the nanosheet expected from that of the $SrNb_2O_6F^-$ layer unit of the precursor. Thus, the exfoliated nanosheet is denoted as "$SrNb_2O_6F^-$ nanosheet" in the rest of the paper. In addition, the concentration of the nanosheet suspension was estimated to be 0.0068 M of $SrNb_2O_6F^-$ based on the Nb content, and it was 71% of the theoretical yield. It is expected that some amount of the exfoliated nanosheets, particularly the larger ones, was precipitated and not collected completely during the centrifugation process of the as-prepared nanosheet suspension. Thus, the exfoliation rate was likely higher than 71%.

A topographic image and a cross-sectional profile of the $SrNb_2O_6F^-$ nanosheets obtained by AFM are shown in Figure 6. The majority of observed nanosheets have lateral sizes

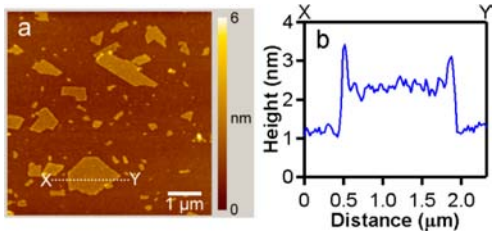

Figure 6. (a) AFM image and (b) cross-section profile of the $SrNb_2O_6F^-$ nanosheets deposited on a Si substrate.

ranging from 0.5 to 2.5 μm. The height of the middle part of the $SrNb_2O_6F^-$ nanosheets is 1.1(1) nm, but the height of the edge parts is as high as 2.0(3) nm after the subtraction of the background height. The similar difference between the edge and the middle part heights has been observed in the other perovskite-type nanosheets prepared from a bulk layered compound $Li_2Ln_{2/3}Ta_2O_7$ (Ln = La, Eu).[30] It is not likely that only the edge part of the nanosheets is not unilamellar. Thus, this behavior is likely originating from water molecules and/or counterions, such as TBA^+, H^+, and H_3O^+, selectively gathered at the edge part. The middle part height of the $SrNb_2O_6F^-$ nanosheets is very close to that expected from the crystal structure of $RbSrNb_2O_6F$ bulk layered precursor (1.09 nm),[25] indicating their homogeneously unilamellar nature. The height of oxide nanosheets observed by AFM tends to be higher than that expected from the crystal structures of their precursors because of water molecules and/or counterions existing on the surface of the nanosheets.[14,32] This aspect suggests that the $SrNb_2O_6F^-$ nanosheet has higher tendency to attract water molecules and/or counterions at its edge part than most of other types of oxide nanosheets.

Figure 7 shows the TEM image (panel a) and SAED pattern (panel b) of the $SrNb_2O_6F^-$ nanosheets. The majority of the observed nanosheets have lateral sizes ranging 0.2 to 1 μm. A slight difference in the size distribution between the AFM and TEM samples is attributed to the difference in the sample

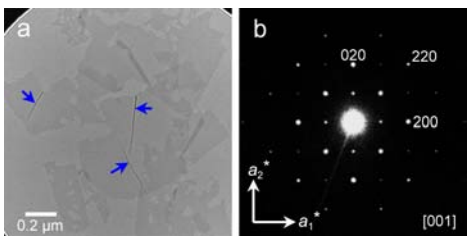

Figure 7. (a) TEM image and (b) SAED pattern of $SrNb_2O_6F^-$ nanosheets.

dx.doi.org/10.1021/ic3022276 | Inorg. Chem. 2013, 52, 415−422

preparation methods. The exceedingly faint and monotonic contrast of the sheet images reflects the ultrathin nature and uniform thickness of the homogeneously unilamellar nanosheets. Line-like features indicated by blue arrows in the figure showed higher contrast, indicating the wrinkled portions of the nanosheets. This suggests that the $SrNb_2O_6F^-$ nanosheet is quite flexible. The SAED pattern of a single nanosheet exhibits sharp diffraction spots, indicating the single crystalline nature of the nanosheet. The diffraction spots of the single nanosheet were indexed well to the square-type cell where no difference in two of the orthogonal lattice parameters along in-sheet directions (*a*- and *b*- axes) was observed within the experimental resolution limit. The estimated lattice parameter of the nanosheet along the in-sheet direction is a = 0.40 nm, which is close to those of the bulk precursors. These results suggest that the exfoliation reaction was topotactic, and the nanosheet product retained the perovskite-type layer unit of their bulk precursors.

Figure 8 (red trace) shows the X-ray scattering profile of the concentrated glue-like nanosheet suspension obtained by high-speed centrifugation of the colloidal nanosheet suspension. The scattering profile mainly consists of a few broad humps overlapped with several sharp peaks reminiscent of the scattering profiles of other soft-chemically exfoliated homogeneously unilamellar nanosheets.[31,33] The sharp peaks can be indexed based on a typical O−Nb−O distance in perovskite-type structures as a lattice parameter, and the refined lattice parameter was a = 0.387(1) nm. This result again indicates that the exfoliated nanosheets retained the perovskite-type structural feature of their bulk precursor. The broad humps are characteristic of a particular structure type of nanosheets.[5,31,33−38] The blue and light-blue dotted traces in Figure 8 represent the product of L_p (Lorentz-polarization factor) and the square of F_{00l} (structure factor of the unilamellar $SrNb_2O_6F^-$ nanosheet) as in

$$I_{00l} = L_p |F_{00l}|^2 = \frac{1 + \cos^2 2\theta}{\sin^2 \theta \cos \theta} |F_{00l}|^2$$

F_{00l} was calculated using the simplified structure model based on the atomic positions in the $SrNb_2O_6F^-$ layer of $RbSrNb_2O_6F$[25] as depicted in Figure 9 and the function

$$F_{00l} = \sum_i m_i f_i \cos[2\pi(2z_i \sin\theta/\lambda)]$$

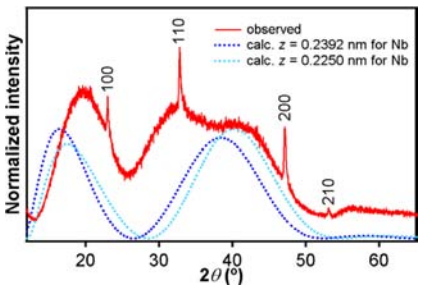

Figure 8. X-ray scattering profile of the concentrated glue-like $SrNb_2O_6F^-$ nanosheet suspension (red trace). The blue and light-blue dotted traces are calculated scattering profiles based on the unilamellar $SrNb_2O_6F^-$ layer model (Figure 9) with different positions of Nb perpendicular to the layer.

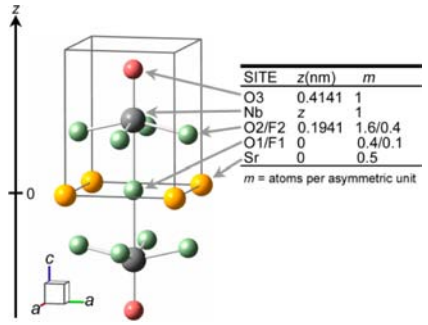

Figure 9. Partial structure model of $SrNb_2O_6F^-$ layer used in the calculation of the X-ray scattering profile of unilamellar $SrNb_2O_6F^-$ nanosheets. The gray frame indicates the asymmetric unit.

where m_i, f_i, z_i, and λ are the site multiplicity, atomic scattering factor, atomic position along the interlayer direction (*c*-axis) of the *i*-th atom, and the X-ray wavelength, respectively. Only the real part of the structure factor was considered because the layer (nanosheet) model is centrosymmetric. In the structure of the precursor $RbSrNb_2O_6F$, Nb is away from the equatorial O2/F2 sites (z = 0.2392 nm). The scattering profile calculated with this Nb position (blue dotted trace) roughly matches with the experimental broad profile, indicating that the nanosheets are homogeneously unilamellar. In addition, it again indicates that the nanosheet fundamentally retains the perovskite-type unit of the precursor. The mismatch in the profiles around 20 to 40° in 2θ is attributed to the diffraction halo from water because it is expected exactly in this range.[39] However, the broad scattering profile calculated with this Nb position was slightly shifted from the experimental one. It is well-known that the distortion degree of NbO_6 octahedra in layered perovskite-type oxides differs when their interlayer cationic species are different.[25] Such structural distortion is attributed to the difference in electrostatic interaction between the layer-unit constituents and interlayer cations for the bulk layered compounds or counter cations for the exfoliated nanosheets. Thus, it is rational to expect that the distortion of F^--incorporated NbO_6 octahedra in the exfoliated $SrNb_2O_6F^-$ nanosheet is slightly different from that in its bulk precursor $RbSrNb_2O_6F$. In the structure of $RbSrNb_2O_6F$, the z coordinate of Nb is unusually shifted from the equatorial O position compared with other Nb-based layered perovskite-type compounds such as $KLaNb_2O_7$.[40] Therefore, we also calculated the scattering profile of $SrNb_2O_6F^-$ layer unit with Nb closer to the equatorial O2/F2 sites (z = 0.2250 nm). The resulting profile (light-blue dotted trace) is closer to the experimental one, suggesting a possible difference in the F^--incorporated NbO_6 octahedra distortion between the $SrNb_2O_6F^-$ nanosheet and its bulk precursor among various other coexisting possibilities such as displacement of O^{2-}. Furthermore, it has been reported that exfoliation of $Cs_{0.7}Ti_{1.825}\square_{0.175}O_4$ ($\square$ = vacancy) into $Ti_{0.91}O_2^{0.36-}$ nanosheet causes the distortion of its Ti−O octahedra and approximately 4% expansion of the layer thickness because of the modification of the electrostatic interaction between the layer-unit constituents and interlayer cations upon exfoliation.[41] Such possible expansion or contraction of the thickness of the exfoliated nanosheet compared with that of the layer unit of the precursor might be another factor for the difference between the observed and the calculated scattering profiles.

dx.doi.org/10.1021/ic3022276 | Inorg. Chem. 2013, 52, 415−422

Figure 10 shows the XRD profile of a sample obtained by drying the concentrated glue-like nanosheet suspension in air.

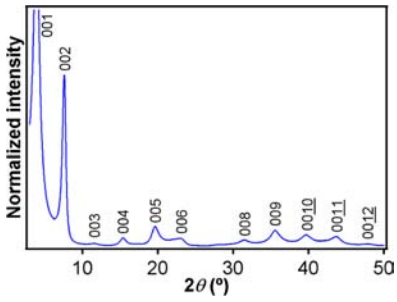

Figure 10. XRD profile of a dried $SrNb_2O_6F^-$ nanosheet suspension on a slide glass.

All the observed peaks can be indexed as 00*l* reflections, indicating the restacking of the nanosheets at a spacing of 2.28(1) nm. No reflection from the in-layer *d*-spacing was observed. These results indicate that the nanosheets in the dried sample were perfectly aligned parallel to the substrate. Highly anisotropic sheet-like morphology of the nanosheets must have caused this organization. The interlayer spacing was much larger than the thickness of the $SrNb_2O_6F^-$ nanosheet expected from the crystal structures of their precursors. This is likely due to the high degree of interlayer hydration in addition to the interlayer incorporation of TBA^+ ions.

UV−vis absorption spectra of the diluted $SrNb_2O_6F^-$ nanosheet suspensions are shown in Figure 11. The optical

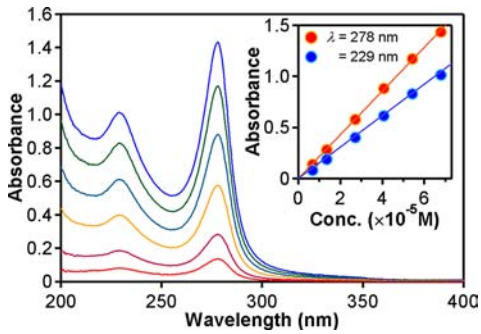

Figure 11. UV−vis absorption spectra of diluted $SrNb_2O_6F^-$ nanosheet suspensions. Absorbance increases linearly as the concentrations of the nanosheet suspensions increase as 6.8×10^{-6} (red trace), 1.4×10^{-5}, 2.7×10^{-5}, 4.1×10^{-5}, 5.4×10^{-5}, and 6.8×10^{-5} M (blue trace). (Inset) Absorbance at 229 and 278 nm plotted against concentrations of the nanosheet suspensions.

absorption edge of the nanosheet was observed around at 293 nm, and two well-defined peaks with their maxima at 229 and 278 nm were observed. These features are quite different from those of perovskite-type oxide nanosheets without F^-, such as $LnNb_2O_7^-$ nanosheets (Ln = La^{3+}, Eu^{3+}, Sm^{3+}).[14,23,24] In case of the $LnNb_2O_7^-$ nanosheets, their absorption edges range between 340 and 370 nm; thus, those are at much longer wavelength than that of the $SrNb_2O_6F^-$ nanosheet. In addition, absorption peaks of $LnNb_2O_7^-$ nanosheets are quite broad and not well-defined. These differences in the absorption spectra between $LnNb_2O_7^-$ and $SrNb_2O_6F^-$ nanosheets suggest that F^- is truly in the crystal structure of the $SrNb_2O_6F^-$ nanosheet and contributing to its characteristic optical properties. The molar extinction coefficients of the $SrNb_2O_6F^-$ nanosheet at 229 and 278 nm were estimated to be $1.54(2) \times 10^4$ and $2.14(2) \times 10^4$ M^{-1} cm^{-1}, respectively. These values are in the same order as those of the basically isostructural $LnNb_2O_7^-$ nanosheets.[14,23]

Figure 12 shows fluorescence spectra of a $SrNb_2O_6F^-$ nanosheet suspension. When this nanosheet was excited with

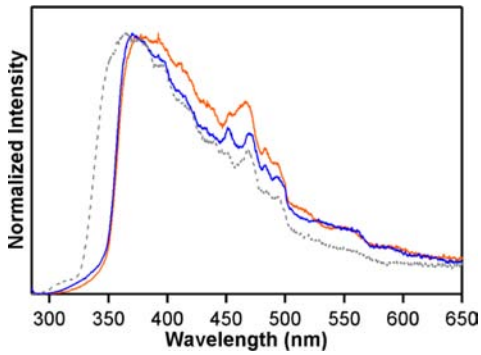

Figure 12. Fluorescence spectra of the $SrNb_2O_6F^-$ nanosheet suspension excited at 229 (red trace) and 278 (blue trace) nm along with that of the $LaNb_2O_7^-$ nanosheet suspension excited at 232 nm (gray dotted trace).

UV light, whose wavelength was below its absorption edge, a broad emission peak with the maximum around 380 nm was observed at room temperature. Nb−F charge transfer transitions as the origin of the emission are not likely in this system because the Nb−F transitions are expected to be situated in the vacuum ultraviolet region in the view of the high optical electronegativity of the F^- ion.[42−44] Thus, the emission is likely originated from Nb−O charge transfer transitions. Similar fluorescence emission was also observed for the $LaNb_2O_7^-$ nanosheet that is a similar perovskite-type oxide nanosheet without F^- ion. However, the emission peak of the $SrNb_2O_6F^-$ nanosheet was narrower than that of the $LaNb_2O_7^-$ nanosheet because the emission intensity of the former below 350 nm was very low. On the other hand, the $LaNb_2O_7^-$ nanosheet exhibits relatively high emission intensity even at 335 nm. The F^--incorporated NbO_6 octahedra in $RbSrNb_2O_6F$ are highly distorted compared with those in layered perovskite-type oxides without F^-.[25] Such a structural feature is also expected in the exfoliated $SrNb_2O_6F^-$ nanosheet. In addition, the electronegativity and crystal field strength of F^- and O^{2-} are significantly different. These features of the oxyfluoride nanosheet might indirectly influence the Nb−O charge transfer property through modification of the electronic structure of the system and cause the difference in the fluorescence properties between the oxyfluoride and the oxide nanosheets even though the confirmation of their mechanism requires further investigation.

These differences between oxyfluoride and oxide nanosheets suggest the capability of anion-site replacement of oxide nanosheets to tune or induce various properties. Replacement of the O^{2-}-site has various potential advantages for oxide nanosheets as functional nanomaterials and nanobuilding blocks. For example, oxyfluorides tend to be better matrixes for rare-earth ion based frequency upconversion materials.[45,46] This is because the lower phonon energy of the (oxy)fluoride matrix tends to reduce nonradiative relaxation energy loss in the rare-earth ion based upconversion materials. Thus, the F^--

dx.doi.org/10.1021/ic3022276 | *Inorg. Chem.* 2013, 52, 415−422

incorporated nanosheets are likely good matrixes for upconversion nanomaterials or nanobuilding blocks.

Also, the aliovalent replacement of the O^{2-} site is interesting and important. For example, it can be utilized to enhance the dielectric property of oxide nanosheets. Several types of oxide nanosheets are known to possess very high dielectric constants regardless of their extremely thin morphology.[12] It is expected that Ti^{4+}-containing nanosheets exhibit even a higher dielectric constant compared with that of solely Nb^{5+}- or Ta^{5+}-based oxide nanosheets.[47] However, on the contrary to the Nb^{5+}- or Ta^{5+}-based layered perovskites, Ti^{4+}-based layered perovskites, which can be exfoliated into homogeneously unilamellar nanosheets, are limited. To solve such an issue, it should be possible to substitute Nb^{5+} or Ta^{5+} of layered perovskites, which can be exfoliated into homogeneously unilamellar nanosheets, with Ti^{4+} if O^{2-} is also simultaneously substituted with F^- to maintain charge neutrality and, thus, the phase stability of the system. Such Ti^{4+}-containing oxyfluoride nanosheets are expected to show superior dielectric performance.

Furthermore, in the view of crystal field strength, by substituting O^{2-} sites of oxide nanosheets with F^-, whose crystal field is weaker than that of O^{2-}, tuning of various physical properties, such as magnetism (high spin versus low spin) and optical absorption and emission, should be possible. Therefore, the results of this preparation of a soft-chemically exfoliated homogeneously unilamellar oxyfluoride nanosheet open the new fascinating field to explore mixed-anion nanosheets as nanomaterials or nanobuilding blocks for a fundamental understanding of the materials and their practical applications. Furthermore, controlling the amount of F^- in such a system will be important. As a plausible approach in such F^- amount control in oxyfluoride nanosheets, the extended research works on the synthesis and exfoliation of $ALa_{1-x}B_xNb_{2-y}Ti_yO_{7-x-y}F_{x+y}$ (A = alkali metal; B = Ca, Sr) and related phases are underway.

■ ASSOCIATED CONTENT

Ⓢ Supporting Information

Elemental composition analysis procedures for the protonated bulk layered precursors and exfoliated nanosheets. This material is available free of charge via the Internet at http://pubs.acs.org..

■ AUTHOR INFORMATION

Corresponding Author

*E-mail: OZAWA.Tadashi@nims.go.jp.

Notes

The authors declare no competing financial interest.

■ ACKNOWLEDGMENTS

We thank K. Takada for use of his research facility and K. Kurashima for preliminary TEM observation of the nanosheet product. This work was in part supported by World Premier International Research Center Initiative on Materials Nanoarchitectonics (WPI-MANA), MEXT, Japan, and CREST of JST. The schematic crystal structures in Figures 2 and 9 were drawn using "Balls & Sticks," free software for crystal structure visualization.[48]

■ REFERENCES

(1) Murphy, D. W.; Hull, G. W., Jr. *J. Chem. Phys.* **1975**, *62*, 973.
(2) Jacobson, A. J. *Mater. Sci. Forum* **1994**, *152*−*153*, 1.
(3) Treacy, M. M. J.; Rice, S. B.; Jacobson, A. J.; Lewandowski, J. T. *Chem. Mater.* **1990**, *2*, 279.
(4) Geim, A. K.; Novoselov, K. S. *Nat. Mater.* **2007**, *6*, 183.
(5) Sasaki, T.; Watanabe, M.; Hashizume, H.; Yamada, H.; Nakazawa, H. *J. Am. Chem. Soc.* **1996**, *118*, 8329.
(6) Ma, R.; Sasaki, T. *Adv. Mater.* **2010**, *22*, 5082.
(7) Ma, R.; Bando, Y.; Sasaki, T. *J. Phys. Chem. B* **2004**, *108*, 2115.
(8) Wang, L.; Sasaki, T.; Ebina, Y.; Kurashima, K.; Watanabe, M. *Chem. Mater.* **2002**, *14*, 4827.
(9) Li, L.; Ma, R.; Iyi, N.; Ebina, Y.; Takada, K.; Sasaki, T. *Chem. Commun.* **2006**, 3125.
(10) Akatsuka, K.; Haga, M.; Ebina, Y.; Osada, M.; Fukuda, K.; Sasaki, T. *ACS Nano* **2009**, *3*, 1097.
(11) Osada, M.; Sasaki, T. *J. Mater. Chem.* **2009**, *19*, 2503.
(12) Osada, M.; Sasaki, T. *Adv. Mater.* **2012**, *24*, 210.
(13) Coleman, J. N.; Lotya, M.; O'Neill, A.; Bergin, S. D.; King, P. J.; Khan, U.; Young, K.; Gaucher, A.; De, S.; Smith, R. J.; Shvets, I. V.; Arora, S. K.; Stanton, G.; Kim, H.-Y.; Lee, K.; Kim, G. T.; Duesberg, G. S.; Hallam, T.; Boland, J. J.; Wang, J. J.; Donegan, J. F.; Grunlan, J. C.; Moriarty, G.; Shmeliov, A.; Nicholls, R. J.; Perkins, J. M.; Grieveson, E. M.; Theuwissen, K.; McComb, D. W.; Nellist, P. D.; Nicolosi, V. *Science* **2011**, *331*, 568.
(14) Ozawa, T. C.; Fukuda, K.; Akatsuka, K.; Ebina, Y.; Kurashima, K.; Sasaki, T. *J. Phys. Chem. C* **2009**, *113*, 8735.
(15) Osada, M.; Ebina, Y.; Fukuda, K.; Ono, K.; Takada, K.; Yamaura, K.; Takayama-Muromachi, E.; Sasaki, T. *Phys. Rev. B* **2006**, *73*, 153301.
(16) Tsujimoto, Y.; Yamaura, K.; Takayama-Muromachi, E. *Appl. Sci.* **2012**, *2*, 206.
(17) Ozawa, T. C.; Kauzlarich, S. M. *Sci. Technol. Adv. Mater.* **2008**, *9*, 033003.
(18) Maeda, K.; Teramura, K.; Lu, D.; Takata, T.; Saito, N.; Inoue, Y.; Domen, K. *Nature* **2006**, *440*, 295.
(19) Toda, K.; Ohtake, N.; Kawakami, M.; Tokuoka, S.; Uematsu, K.; Sato, M. *Jpn. J. Appl. Phys.* **2002**, *41*, 7021.
(20) Liu, G.; Wang, L.; Sun, C.; Chen, Z.; Yan, X.; Cheng, L.; Cheng, H.-M.; Lu, G. Q. *Chem. Commun.* **2009**, 1383.
(21) Xiang, Q.; Yu, J.; Jaroniec, M. *Phys. Chem. Chem. Phys.* **2011**, *13*, 4853.
(22) Kobayashi, Y.; Tian, M.; Eguchi, M.; Mallouk, T. E. *J. Am. Chem. Soc.* **2009**, *131*, 9849.
(23) Ozawa, T. C.; Fukuda, K.; Akatsuka, K.; Ebina, Y.; Sasaki, T. *Chem. Mater.* **2007**, *19*, 6575.
(24) Li, B.-W.; Osada, M.; Ozawa, T. C.; Ma, R.; Akatsuka, K.; Ebina, Y.; Funakubo, H.; Ueda, S.; Kobayashi, K.; Sasaki, T. *Jpn. J. Appl. Phys.* **2009**, *48*, 09KA15.
(25) Choy, J.-H.; Kim, J.-Y.; Kim, S.-J.; Sohn, J.-S.; Han, O. H. *Chem. Mater.* **2001**, *13*, 906.
(26) Appleman, D. E.; Evans, H. T., Jr. *Indexing and Least-Squares Refinement of Powder Diffraction Data (Job 9214)*, U.S. Geological Survey Computer Contribution No. 20, PB; National Technical Information Service: Springfield, VA, 1973; p 60.
(27) Sasaki, T.; Ebina, Y.; Watanabe, M.; Decher, G. *Chem. Commun.* **2000**, 2163.
(28) Fukuda, K.; Kato, H.; Sugimoto, W.; Takasu, Y. Layer-by-Layer Self-Assembly of Unilamellar Nanosheet Crystallites of Ruthenium Oxides. In *Proceedings of the 2009 MRS Fall Meeting*, Boston, MA, May 17, 2009; Materials Research Society: Warrendale, PA, 2009.
(29) Sato, J.; Kato, H.; Kimura, M.; Fukuda, K.; Sugimoto, W. *Langmuir* **2010**, *26*, 18049.
(30) Ozawa, T. C.; Fukuda, K.; Ebina, Y.; Kosuda, K.; Sato, A.; Michiue, Y.; Kurashima, K.; Sasaki, T. *Sci. Technol. Adv. Mater.* **2011**, *12*, 044601.
(31) Ozawa, T. C.; Fukuda, K.; Akatsuka, K.; Ebina, Y.; Sasaki, T.; Kurashima, K.; Kosuda, K. *J. Phys. Chem. C* **2008**, *112*, 17115.
(32) Ozawa, T. C.; Fukuda, K.; Akatsuka, K.; Ebina, Y.; Sasaki, T.; Kurashima, K.; Kosuda, K. *J. Phys. Chem. C* **2008**, *112*, 1312.

(33) Ebina, Y.; Sasaki, T.; Watanabe, M. *Solid State Ionics* **2002**, *151*, 177.
(34) Omomo, Y.; Sasaki, T.; Wang, L.; Watanabe, M. *J. Am. Chem. Soc.* **2003**, *125*, 3568.
(35) Sasaki, T.; Watanabe, M. *J. Am. Chem. Soc.* **1998**, *120*, 4682.
(36) Liu, Z.; Ma, R.; Osada, M.; Iyi, N.; Ebina, Y.; Takada, K.; Sasaki, T. *J. Am. Chem. Soc.* **2006**, *128*, 4872.
(37) Li, L.; Ma, R.; Ebina, Y.; Iyi, N.; Sasaki, T. *Chem. Mater.* **2005**, *17*, 4386.
(38) Walker, J. R. An Introduction to Computer Modeling of X-Ray Powder Diffraction Patterns of Clay Minerals: A Guided Tour of NEWMOD. In *Computer Applications to X-Ray Powder Diffraction Analysis of Clay Minerals*; Reynolds, R. C., Jr., Walker, J. R., Eds.; The Clay Minerals Society: Boulder, CO, 1993; Vol. *5*, p 2.
(39) Stewart, G. W. *Phys. Rev.* **1931**, *37*, 9.
(40) Sato, M.; Abo, J.; Jin, T.; Ohta, M. *J. Alloys Compd.* **1993**, *192*, 81.
(41) Fukuda, K.; Nakai, I.; Oishi, C.; Nomura, M.; Harada, M.; Ebina, Y.; Sasaki, T. *J. Phys. Chem. B* **2004**, *108*, 13088.
(42) Blasse, G.; Dirksen, G. J.; Crosnier-Lopez, M. P.; Fourquet, J. L. *Solid State Commun.* **1994**, *90*, 595.
(43) Blasse, G. *Struct. Bonding (Berlin)* **1980**, *42*, 1.
(44) Shriver, D. F.; Atkins, P. W.; Langford, C. H. Charge-Transfer Bands. In *Inorganic Chemistry*; Oxford University Press: Oxford, U.K., 1990; p 446.
(45) Wang, Y.; Ohwaki, J. *Appl. Phys. Lett.* **1993**, *63*, 3268.
(46) Hua, Y.; Li-Juan, Z.; Jie, M.; Qin, L.; Xuan-Yi, Y.; Bai-Quan, T.; Jing-Jun, X. *Chin. Phys.* **2005**, *14*, 1799.
(47) Osada, M.; Takanashi, G.; Li, B.-W.; Akatsuka, K.; Ebina, Y.; Ono, K.; Funakubo, H.; Takada, K.; Sasaki, T. *Adv. Funct. Mater.* **2011**, *21*, 3482.
(48) Ozawa, T. C.; Kang, S. J. *J. Appl. Crystallogr.* **2004**, *37*, 679.